Published in final edited form as:
*Neuroimage*. 2009 March 1; 45(1): 17–28. doi:10.1016/j.neuroimage.2008.11.010.

# Loss of cerebral white matter structural integrity tracks the gray matter metabolic decline in normal aging⋆

**P. Kochunov**[a,*], **A.E. Ramage**[a], **J.L. Lancaster**[a], **D.A. Robin**[a], **S. Narayana**[a], **T. Coyle**[b], **D.R. Royall**[c], and **P. Fox**[a]

[a]Research Imaging Center, University of Texas Health Science Center, 7703 Floyd Curl Drive, San Antonio, Texas 78284, USA

[b]Department of Psychology, University of Texas at San Antonio, USA

[c]Department of Psychiatry, University of Texas Health Science Center at San Antonio, USA

## Abstract

Relationships between structural MRI-based markers of declining cerebral integrity, and regional PET measurements of $^{18}$FDG uptake have not been studied well in normal aging. In this manuscript we relate changes in cerebral morphology to regional cerebral glucose uptake for 14 major cortical areas in 19 healthy older individuals (age 59–92 years). Measurements of cerebral integrity included gray matter (GM) thickness, sulcal and intergyral spans, fractional anisotropy (FA) of water diffusion and volume of hyperintense WM (HWM) lesions. $^{18}$FDG-PET measurements were converted to standard uptake values and corrected for partial volume artifact. Following this, cortical FDG uptake was significantly correlated with several indices of WM integrity that we previously observed to be sensitive to cognitive decline in executive function, including intergyral span and HWM volumes. Our findings suggest that the age-related decline in white matter integrity, observed as increases in HWM lesions, intergyral spans and reduction in FA, correlated with a decline in the global and regional cerebral glucose uptake. Our findings support the emerging consensus that WM integrity indices are sensitive predictors of declining cerebral health in normal aging. Specifically, age-related WM degradation in the thinly myelinated association tracts appears to track the decreases in global and regional rates of glucose uptake.

## Introduction

A recent review of current and future uses of neuroimaging in the diagnosis of cognitive impairment and dementia reported that the progress in multimodal neuroimaging will eventually lead to “brain-check scans capable of determining the risks of cognitive decline” (Small et al., 2008). Comprehensive multimodal imaging, combining MRI, PET, SPEC and other imaging modalities, will provide an opportunity for early detection of these insidious disorders long before clinically-significant decline in cognitive skills occurs. Early detection allows for the development of preventive therapies as “the feasibility of protecting a healthy brain is always greater than trying to repair brain that is already damaged” (Small et al., 2008). Early discrimination between normal aging and dementias will be made based on analysis of *quantitative*, *systematic* and *regionalized* indices of cerebral integrity that will serve

⋆This research was has been supported by National Institute of Biomedical Imaging and Bioengineering (K01 EB006395) grant to P.K.; Research support was provided by the Human Brain Mapping Project, funded jointly by NIMH and NIDA (P20 MH/DA52176) and by the General Clinical Research Core (HSC19940074H).



*Corresponding author. Fax: +1 210 567 8152. *E-mail address:* kochunov@uthscsa.edu (P. Kochunov).

as surrogate biomarkers for these disorders (Herholz et al., 2002; Reiman et al., 2001; Small, 2006; Thal, 2006). Consequently, multimodal imaging of cerebral alterations occurring during healthy aging or cognitive disorders is an extremely active area of research, where advances in neuroimaging technology are paving the way for quantitative and systematic studies of changes integrity. In fact, a recent multi-center NIH Alzheimer's Disease Neuroimaging Initiative (ADNI), included $^{18}$FDG PET and structural MRI measurements into the standard subject assessment battery (Mueller et al., 2005).

Our group has developed MR-based indices of cerebral integrity that may serve as biomarkers of aging and disease (Kochunov et al., 2005b, 2007, 2008, in press). We found that the age-related trends among these markers were helpful in detailing neuroanatomical and neuropsychological changes with age, providing complimentary information from multiple perspectives (Kochunov et al., 2005b, 2007, 2008, in press). Our present emphasis focuses on exploration of the relationships between specific MR-based measurements of cerebral integrity, which are gray matter (GM) thickness, intergyral and sulcal spans, fractional anisotropy (FA), volume of T2-hyperintense white matter (HWM) and cerebral $^{18}$FDG PET uptake.

Reduced cortical GM thickness is the most studied regional index of declining cortical integrity. In normal subjects, the average thickness of the gray matter mantle is reported to follow an inverted U trajectory with age. That is, GM thickness rises during maturation, reaching its maximum during the 2nd and 3rd decades of life and then linearly decreases with age (Kochunov et al., 2008, 2007; Magnotta et al., 1999; Raz et al., 1997). During normal aging, changes in GM thickness are regionally heterogenous and are more prominent in multi-modal processing regions such as superior and medial frontal areas, than in primary motor or sensory regions (Chetelat et al., 2008; Flood and Coleman, 1988; Kalpouzos et al., 2009; Kochunov et al., 2005b; Morrison and Hof, 1997). Importantly, the rate of cortical GM thickness reduction in neurodegenerative disorders could be different from that in healthy aging and this difference could be an important diagnostic factor (Thompson et al., 2003, 2004).

Increased sulcal and intergyral spans are alsowell-studied regional indices of cerebral integrity. Increases in sulcal span are thought to be a combined result of reduced GM thickness and reduced gyral WM volumes (Bastos Leite et al., 2004; Jernigan et al., 2001; Kochunov et al., 2005b; Magnotta et al.,1999; Symonds et al.,1999). Intergyral span tracks changes in the gyral WM volume that forms the bulk of cortical gyri (Kochunov et al., 2005b, in press). Sulcal and intergyral spans are sensitive to both maturation and senescence of cerebral WM. Both indices follow a “U” trajectory during lifespan, decreasing during maturation, reaching minimum in the 3rd and 4th decades of life and then increasing during senescence (Kochunov et al., in press).

Reduced fractional anisotropy (FA) of water diffusion is a sensitive index of regional breakdown of the micro-structural integrity of cerebral WM tracts (Basser, 1994; Conturo et al., 1996; Pierpaoli and Basser, 1996; Ulug et al., 1995). FA measurements were shown to track progression of demyelinating disorders such as multiple sclerosis, lupus and leukoaraiosis (Horsfield and Jones, 2002). During lifespan, FA follows an inverted “U” trajectory, increasing during maturation, reaching maximum during 3rd–4th decades of life and then decreasing during senescence (Abe et al., 2002; Lehmbeck et al., 2006; Moseley, 2002; Salat et al., 2005; Sullivan and Pfefferbaum, 2003). During senescence, the decline in cerebral FA was shown to be regionally heterogenous. Highest rates of decline were reported for the thinly myelinated associative tracts, while lowest rates of decline were observed in the thickly myelinated motor and sensory tracts (Bartzokis et al., 2001, 2003, 2004; Kochunov et al., 2007; Tang et al., 1997).

T2-hyperintense white matter (HWM) lesions, often observed as high signal intensity regions on T2-weighted MR studies, are common in both normal aging and neurodegenerative disorders. HWM lesions are thought to arise from regions of localized accumulation of extra-cellular water, often associated with degradation of the myelin sheath due to non-specific etiology (Pantoni and Garcia, 1995). The prevalence of HWM lesions has been reported to be as high as 60–100% in normal subjects 60 years old and older (de Leeuw et al., 2001, 2005). These lesions appear more often in frontal regions (Fazekas et al., 2005; Raz et al., 2003) and their volume is correlated with global decreases in cerebral blood flow (Kraut et al., 2008; ten Dam et al., 2007), reduction in cerebral WM and GM volumes (Du et al., 2005; Wen et al., 2006) and reduction in global and regional FA values (Kochunov et al., 2007).

Specific regional patterns of the reductions in cortical $^{18}$FDG PET uptake are commonly described in normal aging and in disorders such as various dementias. $^{18}$FDG PET has been used in the study of aging and neurodegenerative disorders for over two decades (Mielke et al., 1998; Reiman et al., 2001; Small et al., 2008). $^{18}$FDG PET can potentially provide accurate measurements of cerebral glucose uptake and serve as neuroimaging index of neurosynaptic activity and neuronal density. $^{18}$FDG PET studies of normal aging report declining glucose uptake in several cortical areas, including anterior cingulate, frontolateral and perisylvian regions (Garraux et al., 1999; Herholz et al., 2002; Kalpouzos et al., 2009; Mielke et al., 1998). Additionally, patients with early stages of Alzheimer's dementia show profound hypometabolism in the posterior cingulate/superior parietal areas (Small et al., 2008). Specific regional patterns of reductions in glucose uptake were also described for the frontotemporal and vascular dementias and other neurodegenerative CNS disorders (Herholz et al., 2002; Mosconi et al., 2008).

Analysis of age-and-disease-related changes in the metabolism requires correction for partial volume effects. For example, prior $^{18}$FDG PET findings of age-related cortical hypometabolism in normal aging resulted from a failure to account for partial volume effects (Ibanez et al., 2004; Yanase et al., 2005). The cortical GM ribbon cannot be fully resolved on PET images causing cortical $^{18}$FDG uptake to be averaged with lower uptake in the nearby CSF and WM. This leads to a falsely low cortical $^{18}$FDG uptake, reduced by a fraction proportional to ratio of the dimensions of the PET voxel to the regional GM thickness (Park et al., 2006; Yanase et al., 2005). We assert that it is necessary to account for this artifact, especially, in the studies of aging and dementia where the age-related reduction in GM thickness can lead to an artificial reduction in reported cortical $^{18}$FDG uptake. Therefore, we carried out a study to test the specific hypothesis that partial volume averaging can produce an artificial age-related reduction in measured cortical uptake and that the relationships between regional $^{18}$FDG uptake and MR-based indices of cerebral integrity can be influenced by partial volume effects.

## Materials and methods

### Subjects

Nineteen (12 females/7 males), normal, healthy, older subjects aged 59–92 years (average age=75.3±6.1 years)were recruited as part of the International Consortium for Brain Mapping project (ICBM) (Mazziotta et al.,1995). Each subject's medical history was reviewed to rule out hypertension, diabetes, endocrinal, neurological and/or psychiatric illnesses. All subjects underwent a comprehensive neurological examination, had their blood pressure measured to rule out hypertension. Subjects performed within the normal range for their respective ages on the following neuropsychological tests of memory, language, motor and executive function: California Verbal Learning Test-II, Rey–Osterrieth Complex Figure Test, The Purdue Pegboard, Symbol Digit Modalities Test, as well as Block Design and Digit Span of WAIS-III[1] (Delis et al., 2000; Meyers and Meyers, 1995; Smith, 1991; Tiffin, 1968; Wechsler,

1997). All experiments were performed with approval from the internal review board (IRB) and all subjects gave informed consent.

## Imaging

All subjects participated in an optimized, multimodality imaging protocol that produced high-resolution $^{18}$FDG-PET, DTI, T1- and T2-weighted images. All imaging was performed at the Research Imaging Center, University of Texas Health Science Center in San Antonio. $^{18}$FDG-PET imaging was performed using a Siemens/CTI HR+ scanner. MR imaging was done on a Siemens 3 T Trio scanner using a high-resolution 8-channel head coil.

**Diffusion weighted imaging—**A Single-shot spin-echo, echo-planar gradient recalled echo, T2-weighted sequence was used to acquire diffusion weighted data with the spatial resolution of 1.7×1.7×3.0 mm. The sequence parameters were TE/TR=87/8000 ms, with 86 diffusion weighted directions and two diffusion weighing values of 0 and 700 s/mm$^2$. The total sequence acquisition time was 12 min.

**T1-weighted imaging—**High-resolution (isotropic 800 μm), high GM-WM contrast (~25%) T1-weighted images were acquired using a retrospective motion-corrected protocol (Kochunov et al., 2006). With this protocol, six full-resolution volumes are acquired using a T1-weighted, 3D TurboFlash sequence with an adiabatic inversion contrast pulse with the following scan parameters: TE/TR/TI = 3.04/2100/785 ms, flip angle=13°. Total scan time was 26 min.

**T2-weighted imaging—**The T2-weighted data was acquired with a high-resolution (isotropic 1 mm), 3D turbo-inversion recovery Fluid Attenuated Inversion Recovery (FLAIR) sequence with the following parameters: TR/TE/TI/Flip angle=5 s, 353 ms, 1.8 s, 180°. This sequence uses a non-selective inversion recovery pulse to prevent CSF pulsation artifacts (Bakshi et al., 2000). Total scan time was 15 min.

**$^{18}$FDG -PET imaging—**All subjects received approximately 18.5*10$^3$ kBq (5 mCi) injection of $^{18}$F-FDG (average injected activity =18.5±3.7* 10$^3$ kBq) while resting, laying supine with eyes closed on the scanner bed. Following a 40 min uptake period, a 10 min attenuation correction transmission scan was performed using a Ge-68 source. Emission imaging was acquired for 20 min in a 3-D acquisition mode. Emission scans were corrected for radioactive decay, scatter and attenuation and reconstructed iteratively using the Hanning filter with a kernel size of 3.0 mm. $^{18}$FDG images were exported as standardized uptake value (SUV) maps by correcting for injected dose and subject's weight ((kBq/ (cc*kg)), and resampled at isotropic 2 mm spacing.

## Image processing

**DTI images—**Processing of DTI data, to produce regional measurements of WM FA values, was published in our previous work (Kochunov et al., 2007). Briefly, DTI images were processed using a tract-based spatial statistics (TBSS) method that is distributed as a part of

[1]Average raw scores, correlation coefficient with age ($r_{age}$) and average age-normalized scores are shown for the following tests: California Verbal Learning Test (average score = 38.7 ± 10.1;$r_{age}$ = − .42; $p$ = 0.1;average age-adjusted $t$-score = 48.8 ± 10.1); Rey–Osterrieth copy (average score = 29.9 ± 3.6; ;$r_{age}$ = − .36; $p$ = 0.2;average age-adjusted score = 32.2 ± 0.6 ); Rey–Osterrieth recall (average score = 12.4 ± 4.9; $r_{age}$ = − .25; $p$ = 0.3;average age-adjusted score = 13.8 ± 2.6); The Purdue Pegboard dominant hand (average completion time = 90.3 ± 22.3sec;$r_{age}$ = .67; $p$ < 0.01; average age-adjusted completion time = 81.4 ± 3.7s); non-dominant hand (average completion time = 97.2 ± 21.0 sec; $r_{age}$ = .52; $p$ = 0.02; average age-adjusted completion time = 87.3 ± 3.4 sec); Symbol Digit Modalities Test (average score = 39.4 ± 7.9; $r_{age}$ = − .79; $p$ < 0.01; average age-adjusted score = 38.1 ± 1.9); Block Design (average score = 33.8 ± 6.4; $r_{age}$ = − .10; $p$ = 0.5;average age-adjusted score = 11.9 ± 2.4); Digit Span (average score = 15.5 ± 5.1; $r_{age}$ = − .48; $p$ = 0.05 average age-adjusted score = 10.2 ± 3.5).

the FSL package for multi-subject analysis of diffusion anisotropy (Smith et al., 2006). First, fractional anisotropy (FA) images were created by diffusion tensor fitting to the raw diffusion data (Smith, 2002). Next, FA images were nonlinearly aligned to the group-wise, minimal-deformation target brain. It was identified by warping all individual brain images in the group to each other (Kochunov et al., 2001). Then, individual FA images were averaged to produce a group-average anisotropy image. This image is used to create a group-wise skeleton of white matter tracts. The skeletonization procedure is a morphological operation, which extracts the medial axis of an object. This procedure encodes the medial trajectory of the white matter fiber-tracts with one-voxel thin sheaths.

Finally, FA images are projected onto the group-wise skeleton of white matter structures. This steps accounts for residual misalignment among individual white matter tracts. For individual images, FA values are analyzed along the normal projection for each point of the skeleton image and the peak value is assigned to the skeleton. This step effectively corrects for misalignment of individual fiber-tracts. The FA values vary rapidly perpendicular to the tract direction but very slowly along the tract direction. By assigning the peak value to the skeleton, this procedure effectively lines up the center of individual white matter tracts. The projection operation is performed under two constraints. A distance map is used to establish search borders for individual tracts. The borders are created by equally dividing the distance between two nearby tracts. Secondly, a multiplicative 20mm full width at half-max Gaussian weighting is applied during the search to limit maximum projection distance from the skeleton.

**T1-weighted images—**Processing of T1-weighted structural data, to produce regional measurements of cortical GM thickness and intergyral and sulcal span, was described in detail elsewhere (Kochunov et al., 2005b, 2008, 2007). The goal of this processing was to measure average GM thickness for 14 primary cortical regions per hemisphere (Table 1). Gyral and sulcal span also were measured for 12 primary and secondary cortical sulci (Table 1).

Briefly, the processing was performed with the following steps (Fig. 1): removal of non-brain tissue (Fig. 1A), registration to the Talairach frame, RF inhomogeneity correction, fully automated brain tissue partial volume segmentation (Fig. 1B), extraction of GM/WM pial surfaces (Figs. 1C, D), extraction, labeling and verification of sulcal surfaces as described by Mangin et al. (2004) (Figs. 1E, F), and segmentation of the cortical landscape into 14 gyral regions as described by Cachia et al. (2003) (Table 1). The sulcal and intergyral span measurements were calculated as described elsewhere (Kochunov et al., 2005b;Kochunov et al., in press;Kochunov et al., 2007) (Fig. 2). Structural measurements for corresponding gyri/sulci were then averaged for both hemispheres.

**T2-weighted images—**Processing of T2-weighted FLAIR images, to measure the volume the of the HWM lesions, was described previously in (Kochunov et al., in press). In short, FLAIR images were pre-processed using the following steps: removal of non-brain tissue, registration to the T1-weighted images/Talairach frame and RF inhomogeneity correction. Two experienced neuroanatomists, independently, performed identification and manual delineation of hyperintense white mater (HWM) lesions with high ($r$=.85) inter-rater reliability. The volume of HWM was calculated for each subject by adding up the volumes of all individual lesions.

## PET image pre-processing

$^{18}$FDG-PET images were pre-processed for cortical surface-based analysis by spatially aligning them to the corresponding high-resolution structural MR images. A chamfer distance registration method provided in BrainVisa (BV) (www.brainvisa.info) was used. Chamfer distance registration is a surface-based spatial alignment technique developed for registration

of $^{18}$FDG-PET/MRI registration. The BV structural MR image processing pipeline extracts two surfaces: one that corresponds to the outer GM surface and the other corresponds to the WM/GM interface. Both of these cortical outlines were also extracted from the PET images to constrain analysis to cortical GM. These GM/WM surface meshes were aligned using a rigid body spatial transformation to give the maximum overlap between the two sets from each modality. PET images were resliced into 800 μm MRI space using a spline interpolation.

**Cortical parcelation—**Automated parcelation of the cortical regions (Cachia et al., 2003) from high-resolution MR images was based on the borders of the primary and secondary cortical sulci. Cortical parcelation was based on the boundaries of 12 primary cortical sulci that were present in all subjects (Table 1). Some gyri were combined into "cortical areas" due to inter-subject variability of individual gyral boundaries (Cachia et al., 2003). These areas include: 1) inferior parietal lobule, composed of supramarginal and angular gyri; 2) lateral occipital area, spanning the entire surface of the lateral occipital lobe and 3) hippocampal area spanning the cortical surface medial to the fusiform sulcus, including the hippocampus, para-hippocampal gyrus and uncus.

**Surface-based analysis of cortical $^{18}$FDG GM uptake—**Cortical $^{18}$FDG PET uptake measurements were calculated using a surface-based analysis before and after correction for partial volume averaging artifact (Park et al., 2006). The partial volume correction (PVC) consisted of two steps: mapping peak cortical $^{18}$FDG uptake values onto the cortical surface derived from the high-resolution MR images and then correcting these values for variability in the regional cortical thickness (Fig. 3).

### Step 1: Mapping of cortical $^{18}$FDG uptake values onto the cortical surface

**Gray matter:** Mapping of peak $^{18}$FDG uptake values in the cerebral cortex was done for each patch of the cortical surface that was identified as a gyrus/cortical area using the high-resolution structural MR processing pipeline (Fig. 3, steps A, C). The mapping assigns each node of a cortical patch the maximum $^{18}$FDG uptake value found along the path normal to the cortical GM ribbon (Fig. 3F). The search for maximum uptake values was performed along the same path that was used to measure cortical GM thickness for this location. This path originates at the WM/GM boundary, runs normal to it and connects to a corresponding location on the outer GM surface (Fig. 3F). The 3D distance between the corresponding locations on the WM/GM boundary and outer GM surface extracted from MR images is recorded as the cortical GM thickness for this node (Fig. 3I). To search for the peak uptake value in the PET image, the path is extended on either end by the distance equal to the GM thickness. The peak cross-sectional cortical $^{18}$FDG uptake value ($A_{max}$) was assumed to represent the intensity that corresponds to the center of the GM ribbon. By extending the path in both directions, this procedure helped to correct for small residual misalignment between the PET and MR images. This search operation was performed under two constraints. First, the path could not be extended into a neighboring GM region (e.g. going into a neighboring gyrus). Second, the PET cross-sectional profile was forced to be a single peak bell-shaped function. This was done by smoothing the PET profiles by a convolution with a Gaussian function with FWHM equal to the regional GM thickness. Profiles with multiple maxima were discarded. These criteria resulted in dropping of 15–25% of the nodes.

**Step 2: Surface-based correction for partial volume artifact—**Partial volume correction (PVC) reduced variability in the cortical $^{18}$FDG uptake values arising from the inter-subject difference in GM thickness. We used a modified surface based PVC technique developed by Park et al. (2006). This technique models an $^{18}$FDG PET image as a convolution between the "true" $^{18}$FDG uptake image and the point spread function (PSF) of the PET scanner (approximated PSF as a Gaussian function with a fixed FWHM). However, this technique

requires an approximation of the PSF as a slowly varying function of the distance from the scanner's isocenter as one of the inputs to accommodate for the parallax effect (Park et al., 2006). Here, we modified this technique by modeling the PSF using information provided by gyral parcelation. This adaptation was based on three assumptions. First, it was assumed that if subjects' head positioning were consistent within the PET scanner, the same gyrus/cortical areas in different subjects would be located at a similar distance from the scanner's isocenter, having similar regional PSF. This supported the assumption that the each gyrus in different subjects experienced similar PV effects. Our second assumption was that the PV effect is predominantly influenced by regional differences in cortical thickness. Third, we assumed that across subjects the gyral uptake value ($A_{max}$) would be highly correlated with the gyral GM thickness. For example, subjects with thicker cortex were expected to have higher $A_{max}$ values, than subjects with thinner cortex. The “true” cross-sectional profile of cortical ribbon uptake values was modeled using two approximations; rectangular and Gaussian (see Appendix 1). Modeling of the three assumptions showed that $A_{max}$ uptake value was nearly linearly related to the regional thickness of the cortical ribbon (Appendix 1).

**Volume-based analysis of subcortical $^{18}$FDG WM uptake—**Average WM $^{18}$FDG uptake values ($A_{wm}$) were calculated for the entire volume of the cerebral WM and for the three regions of corpus callosum (CC). Subjects' WM masks were obtained from the tissue classified MR images (Fig. 1B;Fig. 3B). WM masks were eroded with a spherical, 6 voxel/4.8 mm diameter kernel to reduce partial averaging with the surrounding cortical GM and ventricular CSF uptake values. Subject's average WM $^{18}$FDG uptake value ($A_{wm}$) was calculated by averaging uptake values within individual WM mask. Average $^{18}$FDG uptake was also calculated for three sub-regions of corpus-callosum divided along its anterior–posterior length (Kochunov et al., 2005a) (Fig. 3H). This anterior–posterior CC subdivision schema (Fig. 3 bottom) is popular because commissural WM that forms the CC was shown to have distinct topographic distributions (Aboitiz, 1992;Aboitiz et al., 1992;Highley et al., 1999). The anterior third (genu) of the CC contains the thinly myelinated, tightly packed association fibers connecting the bilateral frontal/anterior cingulate cortices; the midbody (middle third) primarily contains thickly myelinated fibers for motor, somatosensory and auditory cortices and the posterior third (splenium) contains a mixture of heavily myelinated and thinly myelinated fibers connecting the temporal, parietal and occipital lobes (Witelson, 1989). A ten millimeter-wide band of the CC was segmented from the cerebral WM mask and eroded with a spherical kernel with the diameter=5voxels/4 mm (Fig. 3E).

## Results

Average and standard error of the mean (SEM) values for the surface area, average GM thickness, uncorrected and partial volume corrected $^{18}$FDG uptake values and correlation coefficients between GM thickness and $^{18}$FDG uptake values are shown for the fourteen cortical areas in Table 2. On average, the SEM for regional cortical surface areas, GM thickness and $^{18}$FDG uptake values were <10% of the mean value; confirming the high level of intersubject consistency of cortical parcelations and mapping of cortical uptake values (Cachia et al., 2003;Park et al., 2006). The intragyral correlations between $A_{max}$ and gyral GM thickness were significant for every gyrus (Table 2). However, the combined scatter plot for all gyri (Fig. 5, top) showed no significant correlation between uptake values and GM thickness ($r$=.25, $p$>.30). This was due to known regional differences in the baseline metabolism (Ibanez et al., 2004). Fig. 4 indicated that baseline $^{18}$FDG uptake was the highest for the frontal, parietal and occipital areas, while cingulate and hippocampal areas showed the least $^{18}$FDG uptake, similar to findings reported in (Ibanez et al., 2004). To remove the regional variability in baseline metabolism, we value-normalized individual gyral uptake values ($A_{max}$) to the whole brain average cortical uptake value. This correction resulted a significant correlation ($r$=.46, $p$<.01) between $A_{max}$ and GM thickness (Fig. 5, bottom).

The average correlation coefficients between $A_{max}$ and GM thickness were slightly higher for PVC performed using Gaussian and rectangular profile approximations ($r_{Gaus}$ =.52 vs $r_{Rect}$=.50; $p$>.20). Following PVC, there was a significant reduction ($p$<.001) of inter-subject variability for corrected $A'_{max}$ values and the average SEM values were reduced from 5% to 3.6% using Gaussian approximation; (Table 2).

### Correlations between global $^{18}$FDG uptake, age and MR-based indices of cerebral integrity

Uncorrected average cortical $^{18}$FDG uptake ($A_{max}$) was significantly correlated with age ($r_{gm}$=−.54; $p$<.01). This correlation became non-significant following PVC ($A'_{max}$ vs age $r_{rec}$=−.27 and $r_{gaus}$=−.28; $p$>.2; see Fig. 6 and Table 3). Age-independent relationships between $^{18}$FDG uptake values were studied using partial age-corrected correlation analyses. Uncorrected average cortical uptake values were significantly correlated with GM thickness and two MR-based measurements of WM integrity: HWM volume and intergyral span (Table 4). Following PVC, the correlation with GM thickness became non-significant but correlations with HWM volume and intergyral span became numerically stronger (Table 4).

### Correlations between gyral $^{18}$FDG uptake and MR-based indices of cerebral integrity

Correlations between gyral $^{18}$FDG uptake values, age and MR-based integrity indices, before and after PVC were tabulated (Table 5). As PVC correction with Gaussian approximation returned numerically higher correlation coefficients than with rectangular approximation, only $A'_{max/Gauss}$ numbers were shown. The level of statistical significance was set at $p$=.003 ($r$>.65) to reduce the probability of Type 1 errors associated with comparisons across 14 cortical regions. Similar to global trends, age was negatively correlated with $A_{max}$ for every gyral area. Following PVC, age was no longer a significant covariate for the regional $A'_{max/Gauss}$ values; however, non-significant moderate negative correlations ($r$=−.35 to −.42; $p$=.15 to .07) remained for the superior and intermediate frontal gyri, the cingulate gyrus, and the hippocampal area.

Age-independent relationships between corrected cortical $^{18}$FDG PET uptake values and MR-based indices showed that gyral uptake values did not significantly correlate with GM thickness and FA values for any of the regions (Table 5). In contrast, two MR-indices of WM atrophy: HWM volume and intergyral span showed moderate to strong correlation ($r$=−.4 to −.6; $p$=.05 −.01) with the cortical $^{18}$FDG uptake values, however, none were significant, when corrected for multiple comparisons ($p$=.003;$r$>.65).

### Correlations between $^{18}$FDG uptake in the corpus callosum, age and MR-based indices of cerebral integrity

Average $^{18}$FDG uptake was calculated for three regions of the corpus callosum (CC): genu, body and splenium (Fig. 3 bottom). The genu of the CC was the only region where the $^{18}$FDG uptake was significantly correlated with age ($r$=−.63; $p$<.01) (Table 6). Age-corrected correlation analysis showed that regional CC $^{18}$FDG uptake was not significantly correlated with GM thickness. However, $^{18}$FDG uptake values for all three regions were significantly correlated with MR-based WM atrophy indices: HMW volume and intergyral span (Table 7). $^{18}$FDG uptake values for the genu and the splenium were also significantly correlated with FA (Table 7).

Interestingly, the genu was also the only region where the $^{18}$FDG uptake was significantly correlated with the average cortical $^{18}$FDG uptake. The age-corrected correlations for the genu and cortical $^{18}$FDG uptake was $pr$=.56;. and .67 ($p$<.01) for $A_{max}$; and $A'_{max/Gauss}$, respectively (Table 7). The average correlation for the body and splenium were not significant ($pr$=.06;. and .14 and $pr$=.16;.21 and .22).

## Discussion

The combination of quantitative MRI and $^{18}$FDG PET measurements of cerebral integrity holds great potentials in the discrimination of normal aging from earlier stages of cognitive impairment and dementia (Small et al., 2008). The ability to discriminate normal aging from dementia using diverse, multi-modal neuroimaging indices of cerebral integrity requires a sound understanding of factors affecting the indices. This study analyzed relationships between regional $^{18}$FDG uptake and MR-based indices of cerebral integrity in healthy, aging subjects. Low spatial resolution of PET cameras prevents PET images from fully resolving cortical GM ribbon leading to artifactual reductions in cortical uptake values (Appendix 1). These artifacts have been shown to be the cause of several erroneous findings of hypometabolism in aging, dementia and disorders (Ibanez et al., 2004; Inoue et al., 2005; Park et al., 2006).

Our study found that the partial volume averaging can produce an artificial age-related reduction in measured cortical uptake. Uncorrected, average cortical $^{18}$FDG uptake ($A_{max}$) was significantly correlated with age ($r$=−.54; $p$<.01), suggesting age-related hypometabolism. Notably, following partial volume correction (PVC), cortical uptake values were no longer significantly correlated with age (Table 3), consistent with similar studies using PVC (Park et al., 2006;Yanase et al., 2005). Thus, PVC changed the pattern of correlation between cortical $^{18}$FDG uptake and MR-based indices of cerebral integrity, providing more accurate results. Prior to PVC, average cortical $^{18}$FDG uptake was significantly correlated with GM thickness ($r$=.46; $p$<.05), but after PVC this correlation was non-significant (Table 4). In contrast, correlations between cortical $^{18}$FDG uptake and MR-based indices of WM integrity, such as HWM volume and intergyral span became numerically stronger following PVC (Table 4). This generally held true for other regional cortical analyses (Table 5). Prior to PVC, all regional cortical uptake values correlated with age at the level of ($r$=−.45−.6; $p$=.05−.01). Following PVC, there were no significant correlations with age for any region. As expected from global trends, correlations between regional uptake values, HWM volume ($r$=−.44 vs. −.52) and intergyral span ($r$=−.47 vs. −.51) were higher although following PVC though none reached the level of statistical significance necessary for multiple comparisons.

Our data additionally showed significant differences in $^{18}$FDG uptake trends between thinly myelinating associative and heavily myelinated motor WM tracts (Table 6,Table 7). Consistent with previous findings regarding difference in aging trends in WM, only the $^{18}$FDG uptake in the genu of the CC showed a significant correlation with age ($r$= −.63; $p$<.001) (Table 6). The genu of CC is composed of thinly myelinated associative tracts linking higher cognitive areas (Aboitiz et al., 1992). In contrast, uptake values in the body of CC were not correlated with age ($r$=−.3; $p$=~.4). The body of the CC is composed of heavily myelinated motor and sensory tracts connecting primary motor and sensory cortices (Aboitiz et al., 1992). $^{18}$FDG uptake in the genu of CC was also highly correlated with the MR-based indices of WM integrity, even when age corrected (Table 7). Specifically, uptake values in the genu were correlated with HWM and intergyral span e.g. the MR-based indices correlated with the cortical $^{18}$FDG uptake (Table 7). This finding is consistent with the previously reported association between reduction in WM integrity in the genu and hypometabolism in the frontal areas (Inoue et al., 2008). Uptake values in the other partitions of the CC, and the uptake values for the entire WM volume were also significantly correlated with intergyral span and HWM volume, indicating that these two MR indices of WM atrophy are predicative of decline in FDG uptake throughout WM (Table 7).

Following PVC, only HWM volume and intergyral span (our key indices of WM integrity) remained strongly correlated with decline in FDG uptake. The mechanisms by which the decline in WM integrity decreases the cerebral glucose uptake are unknown. It has been postulated that HWM lesions disrupt myelin and cause de-synchronization of the multitude of

cortical networks relying on this complex WM relay system (Bartzokis, 2004; DeCarli et al., 1995). Our findings also supported earlier observations regarding accelerated aging trends in the thinly myelinated associative WM. Previously, it was shown that thinly myelinated, associative tracts, located in the genu of CC, are especially vulnerable to accumulation of metabolic damage and this adversely affects the neurons throughout the cortex due to the loss of neurotrophic factors (Dai et al., 2001; Hildebrand et al., 1993; Inoue et al., 2008; Wilkins et al., 2001, 2003). The finding that $^{18}$FDG uptake in the genu is highly correlated with age, cortical uptake and MR-based indices of atrophy suggests an outward progression of functional decline from thinly myelinated association WM tracts to cerebral cortex.

## Limitations

There are two limitations that impact this manuscript. One limitation was the small number of subjects. This study was explorative in nature, where the age-independent relationships among a wide variety of measurements were studied in relatively few subjects. Typically, this analysis would be performed using exploratory statistical techniques such as principal or independent component analysis (PCA/ICA). However, we could not use these techniques due to the requirements they place on the ratio of dependent variables vs. subject number of at least 1:10 (Osborne and Costello, 2004). The small number of subjects also prevented us from performing multivariate analysis of the regional $^{18}$FDG uptake trends where even moderate correlation values ($r$~.5–.6) are non-significant when corrected for multiple comparisons.

The other main limitation of this study was the use of semi-quantitative analysis of $^{18}$FDG PET uptake with standard uptake values. Fully quantitative $^{18}$FDG-PET measurements based on continuous arterial blood sampling and modeling of cerebral glucose metabolism have been developed over 20 years ago (Fox et al., 1988; Raichle, 1981). However, fully quantitative $^{18}$FDG-PET studies are not routinely performed in clinical work or in large multi-center studies due to complexity associated with continuous arterial blood sampling. For example, the recent multi-center NIH-funded Alzheimer's Disease Neuroimaging Initiative uses standard uptake values to report $^{18}$FDG-PET data (Mueller et al., 2005).

## Conclusion

In this work, we demonstrated the importance of partial volume correction for $^{18}$FDG-PET studies of normal aging. Partial volume correction is necessary to avoid artifactual findings such age-related hypermetabolism and significant correlations with GM thickness. We showed that following PVC, MR-based measurements of WM integrity, e.g. HWM volume and intergyral span, were exclusively related to the decline in cortical uptake values. In other work, from our lab we also showed that the same measurements have also showed significant age-corrected association with the decline in executive control function during normal aging and explained 62% of intersubject variability in the neurocognitive scores (Kochunov et al., in press). The trends and relationships we observed between PET and structural MRI indices added strength to the argument that WM degradation is a major contributor to functional changes observed in normal aging. These data have shed light on the correspondence of indices of WM integrity and the age-related decline in cerebral metabolism. Future work in this area should continue to correct for partial volume artifact while extending exploration into the associations between indices of cerebral integrity, including measurement of regional glucose uptake, and cognitive/behavioral outcomes.

## Abbreviations

$A_{max}$, Maximum cortical FDG uptake value; $A'_{max/Rect}$, Maximum cortical FDG uptake value following partial volume correction using rectangular approximation; $A'_{max/Gaus}$, Maximum

cortical FDG uptake value following partial volume correction using Gaussian approximation; $A_{wm}$, FDG uptake value (activity) in cortical white matter; BV, Brain Visa; GM, Gray Matter; HWM, Hyperintense white matter; PVC, Partial volume correction; WM, White matter.

## Acknowledgments

This work has been supported by the National Institute of Biomedical Imaging and Bioengineering (K01 EB006395) grant to P. K.; Research support was provided by the Human Brain Mapping Project funded by NIMH and NIDA (P20 MH/DA52176), and by the General Clinical Research Core (HSC19940074H).

## Appendix

## Appendix A. Modeling of effects of the GM thickness on the peak PET intensity

Spatial resolution of modern PET cameras is not sufficient to faithfully reproduce the detailed spatial nature of the cortical GM ribbon. This failure is attributed to a partial voxel averaging effect, where the voxel value is the average response over the extent of the PET imager's point spread function (PSF). Since the PSF of PET imagers extend well outside the cortical bounds, voxel values within cortex will be lessened for FDG studies, because surrounding tissues and compartments will have lower FDG concentrations. The thickness of the GM ribbon varies across cortex and thicker GM regions will occupy a larger fraction of the PET PSF and therefore have a higher peak voxel value. We modeled the effect of regional variations in cortical GM thickness on peak voxel values using convolution between the cross-sectional profile of assumed "true" GM FDG uptake profile and the PSF of the PET scanner. The profile of the GM FDG uptake was assumed to follow the cross-sectional profile of GM values measured from a coregistered high-resolution MRI. The true GM FDG uptake profile was modeled using two approximations. In the first approximation we assumed that the true profile was represented by a rectangular function with the width given by the Full-Width-at-Half-Maximum of the MRI measured GM profile ($FWHM_{gm}$). In the second approach, the true GM FDG profile was modeled as a Gaussian function with the same FWHM. The point spread function (PSF) of the PET camera was modeled as a Gaussian function with the $\sigma_{pet}=FWHM_{pet}/2.35$ (Eq. (A.1)

$$\mathrm{PSF}_{\mathrm{pet}}(x;\sigma_{\mathrm{pet}})=\frac{1}{\sigma_{\mathrm{pet}}\cdot\sqrt{2\pi}}e^{\frac{x^2}{2\sigma_{\mathrm{pet}}^2}} \tag{A.1}$$

## Rectangular FDG uptake profile

The "true" cross-sectional FDG profile for a cortical ribbon was approximated by a rectangular function with amplitude A', and width=$FWHM_{gm}$ (Fig. 1A top). The GM profile in the reconstructed FDG PET image was modeled as a convolution between the rectangular cross-sectional profile and PSF of the PET scanner (Fig. 1A top, left). The result of this convolution is a bell-shaped function shown in Fig. 1A top, left. The magnitude A' is related to the reconstructed peak magnitude A of the FDG image as shown in Eq. (2).

$$A' \sim \frac{A}{\int_{-\mathrm{FWHM}_{\mathrm{gm}}/2}^{\frac{\mathrm{FWHM}_{\mathrm{gm}}}{2}} \mathrm{PSF}\ (x,\sigma_{\mathrm{pet}})\,\mathrm{dx}} \tag{A.2}$$

We modeled equation A.2 for the observed range of cortical GM thickness values of 1.7–3.5 mm and expected $FHWM_{pet}$ of the PET camera are in the range of 5–10 mm. Fig. A.1 shows

the A/A' ratio as the function of GM thickness at the $FHWM_{pet}$=6 mm. This relationship can be approximated as a linear function of $FHWM_{gm}$ with an average approximation error<1% (Fig. 1A top).

## Gaussian FDG uptake profile

In the second approach we modeled the "true" cross-sectional FDG profile for the cortical ribbon as a non-normalized Gaussian function with a peak magnitude A' (Eq. A.3), where $\sigma_{gm}=FWHM_{gm}/2.35$. Lack of normalization factor allows us to have same peak intensity for GM ribbon areas of different thickness.

$$G=A' \cdot e^{\frac{x^2}{2\sigma^2_{GM}}} \tag{A.3}$$

The reconstructed FDG PET image was again modeled as a convolution between G and PSF of the PET scanner. The result of this convolution is a Gaussian function shown in Fig. 1A bottom, left. However, once again we are only interested in the ratio between the reconstructed and the original peak magnitudes. This relationship is given by Eq. A.4 and its dependence on the regional GM thickness can be modeled using a linear approximation ($r^2$>0.99) (Fig.1A, bottom, right).

$$A' \sim \frac{A}{\frac{\sigma_{gm}}{\sqrt{\sigma^2_{gm}+\sigma^2_{pet}}}} \tag{A.4}$$

## References


Abe O, Aoki S, Hayashi N, Yamada H, Kunimatsu A, Mori H, Yoshikawa T, Okubo T, Ohtomo K. Normal aging in the central nervous system: quantitative MR diffusion-tensor analysis. Neurobiol. Aging 2002;23:433–441. [PubMed: 11959406]

Aboitiz F. Brain connections: interhemispheric fiber systems and anatomical brain asymmetries in humans. Biol. Res 1992;25:51–61. [PubMed: 1365702]

Aboitiz F, Scheibel AB, Fisher RS, Zaidel E. Fiber composition of the human corpus callosum. Brain Res 1992;598:143–153. [PubMed: 1486477]

Bakshi R, Caruthers SD, Janardhan V, Wasay M. Intraventricular CSF pulsation artifact on fast fluid-attenuated inversion-recovery MR images: analysis of 100 consecutive normal studies. AJNR Am. J. Neuroradiol 2000;21:503–508. [PubMed: 10730642]

Bartzokis G. Age-related myelin breakdown: a developmental model of cognitive decline and Alzheimer's disease. Neurobiol. Aging 2004;25:5–18. [PubMed: 14675724]

Bartzokis G, Beckson M, Lu PH, Nuechterlein KH, Edwards N, Mintz J. Age-related changes in frontal and temporal lobe volumes in men: a magnetic resonance imaging study. Arch. Gen. Psychiatry 2001;58:461–465. [PubMed: 11343525]

Bartzokis G, Cummings JL, Sultzer D, Henderson VW, Nuechterlein KH, Mintz J. White matter structural integrity in healthy aging adults and patients with Alzheimer disease: a magnetic resonance imaging study. Arch. Neurol 2003;60:393–398. [PubMed: 12633151]

Bartzokis G, Sultzer D, Lu PH, Nuechterlein KH, Mintz J, Cummings J. Heterogeneous age-related breakdown of white matter structural integrity: implications for cortical "disconnection" in aging and Alzheimer's disease. Neurobiol. Aging 2004;25:843–851. [PubMed: 15212838]

Basser PJ. Focal magnetic stimulation of an axon. IEEE Trans. Biomed. Eng 1994;41:601–606. [PubMed: 7927380]

Bastos Leite AJ, Scheltens P, Barkhof F. Pathological aging of the brain: an overview. Top Magn. Reson. Imaging 2004;15:369–389. [PubMed: 16041289]

Cachia A, Mangin JF, Riviere D, Papadopoulos-Orfanos D, Kherif F, Bloch I, Regis J. A generic framework for the parcellation of the cortical surface into gyri using geodesic Voronoi diagrams. Med. Image Anal 2003;7:403–416. [PubMed: 14561546]

Chetelat G, Desgranges B, Landeau B, Mezenge F, Poline JB, de la Sayette V, Viader F, Eustache F, Baron JC. Direct voxel-based comparison between grey matter hypometabolism and atrophy in Alzheimer's disease. Brain 2008;131:60–71. [PubMed: 18063588]

Conturo TE, McKinstry RC, Akbudak E, Robinson BH. Encoding of anisotropic diffusion with tetrahedral gradients: a general mathematical diffusion formalism and experimental results. Magn. Reson. Med 1996;35:399–412. [PubMed: 8699953]

Dai X, Qu P, Dreyfus CF. Neuronal signals regulate neurotrophin expression in oligodendrocytes of the basal forebrain. Glia 2001;34:234–239. [PubMed: 11329185]

de Leeuw FE, de Groot JC, Achten E, Oudkerk M, Ramos LM, Heijboer R, Hofman A, Jolles J, van Gijn J, Breteler MM. Prevalence of cerebral white matter lesions in elderly people: a population based magnetic resonance imaging study. The Rotterdam Scan Study. J. Neurol. Neurosurg. Psychiatry 2001;70:9–14. [PubMed: 11118240]

de Leeuw FE, Barkhof F, Scheltens P. Progression of cerebral white matter lesions in Alzheimer's disease: a new window for therapy? J. Neurol. Neurosurg. Psychiatry 2005;76:1286–1288. [PubMed: 16107369]

DeCarli C, Murphy DG, Tranh M, Grady CL, Haxby JV, Gillette JA, Salerno JA, Gonzales-Aviles A, Horwitz B, Rapoport SI, et al. The effect of white matter hyperintensity volume on brain structure, cognitive performance, and cerebral metabolism of glucose in 51 healthy adults. Neurology 1995;45:2077–2084. [PubMed: 7501162]

Delis, C.; Kramer, J.; Kaplan, E.; Ober, B. California Verbal Learning Test-Second Edition. San Antonio: The Psychological Corporation; 2000.

Du AT, Schuff N, Chao LL, Kornak J, Ezekiel F, Jagust WJ, Kramer JH, Reed BR, Miller BL, Norman D, Chui HC, Weiner MW. White matter lesions are associated with cortical atrophy more than entorhinal and hippocampal atrophy. Neurobiol. Aging 2005;26:553–559. [PubMed: 15653183]

Fazekas F, Ropele S, Enzinger C, Gorani F, Seewann A, Petrovic K, Schmidt R. MTI of white matter hyperintensities. Brain 2005;128:2926–2932. [PubMed: 15958507]

Flood D, Coleman P. Neuron numbers and size in aging brain: comparison of human, monkey and rodent data. Neurobiol. Aging 1988;9:453–463. [PubMed: 3145463]

Fox PT, Raichle ME, Mintun MA, Dence C. Nonoxidative glucose consumption during focal physiologic neural activity. Science 1988;241:462–464. [PubMed: 3260686]

Garraux G, Salmon E, Degueldre C, Lemaire C, Laureys S, Franck G. Comparison of impaired subcortico-frontal metabolic networks in normal aging, subcortico-frontal dementia, and cortical frontal dementia. NeuroImage 1999;10:149–162. [PubMed: 10417247]

Herholz K, Salmon E, Perani D, Baron JC, Holthoff V, Frolich L, Schonknecht P, Ito K, Mielke R, Kalbe E, Zundorf G, Delbeuck X, Pelati O, Anchisi D, Fazio F, Kerrouche N, Desgranges B, Eustache F, Beuthien-Baumann B, Menzel C, Schroder J, Kato T, Arahata Y, Henze M, Heiss WD. Discrimination between Alzheimer dementia and controls by automated analysis of multicenter FDG PET. NeuroImage 2002;17:302–316. [PubMed: 12482085]

Highley JR, Esiri MM, McDonald B, Roberts HC, Walker MA, Crow TJ. The size and fiber composition of the anterior commissure with respect to gender and schizophrenia. Biol. Psychiatry 1999;45:1120–1127. [PubMed: 10331103]

Hildebrand C, Remahl S, Persson H, Bjartmar C. Myelinated nerve fibres in the CNS. Prog. Neurobiol 1993;40:319–384. [PubMed: 8441812]

Horsfield MA, Jones DK. Applications of diffusion-weighted and diffusion tensor MRI to white matter diseases — a review. NMR Biomed 2002;15:570–577. [PubMed: 12489103]

Ibanez V, Pietrini P, Furey ML, Alexander GE, Millet P, Bokde AL, Teichberg D, Schapiro MB, Horwitz B, Rapoport SI. Resting state brain glucose metabolism is not reduced in normotensive healthy men during aging, after correction for brain atrophy. Brain Res. Bull 2004;63:147–154. [PubMed: 15130704]

Inoue K, Ito H, Goto R, Nakagawa M, Kinomura S, Sato T, Sato K, Fukuda H. Apparent CBF decrease with normal aging due to partial volume effects: MR-based partial volume correction on CBF SPECT. Ann. Nucl. Med 2005;19:283–290. [PubMed: 16097637]

Inoue K, Ito H, Uchida S, Taki Y, Kinomura S, Tsuji I, Sato S, Horie K, Kawashima R, Ito M, Fukuda H. Decrease in glucose metabolism in frontal cortex associated with deterioration of microstructure of corpus callosum measured by diffusion tensor imaging in healthy elderly. Hum. Brain Mapp 2008;29:375–384. [PubMed: 17450581]

Jernigan TL, Archibald SL, Fennema-Notestine C, Gamst AC, Stout JC, Bonner J, Hesselink JR. Effects of age on tissues and regions of the cerebrum and cerebellum. Neurobiol. Aging 2001;22:581–594. [PubMed: 11445259]

Kalpouzos G, Chetelat G, Baron JC, Landeau B, Mevel K, Godeau C, Barre L, Constans JM, Viader F, Eustache F, Desgranges B. Voxel-based mapping of brain gray matter volume and glucose metabolism profiles in normal aging. Neurobiol. Aging 2009;30(1):112–124. [PubMed: 17630048]

Kochunov P, Lancaster JL, Thompson P, Woods R, Mazziotta J, Hardies J, Fox P. Regional spatial normalization: toward an optimal target. J. Comput. Assist. Tomogr 2001;25:805–816. [PubMed: 11584245]

Kochunov P, Lancaster J, Hardies J, Thompson PM, Woods RP, Cody JD, Hale DE, Laird A, Fox PT. Mapping structural differences of the corpus callosum in individuals with 18q deletions using targetless regional spatial normalization. Hum. Brain Mapp 2005a;24:325–331. [PubMed: 15704090]

Kochunov P, Mangin JF, Coyle T, Lancaster J, Thompson P, Riviere D, Cointepas Y, Regis J, Schlosser A, Royall DR, Zilles K, Mazziotta J, Toga A, Fox PT. Age-related morphology trends of cortical sulci. Hum. Brain Mapp 2005b;26:210–220. [PubMed: 16161162]

Kochunov P, Lancaster JL, Glahn DC, Purdy D, Laird AR, Gao F, Fox P. Retrospective motion correction protocol for high-resolution anatomical MRI. Hum. Brain Mapp 2006;27:957–962. [PubMed: 16628607]

Kochunov P, Thompson PM, Lancaster JL, Bartzokis G, Smith S, Coyle T, Royall DR, Laird A, Fox PT. Relationship between white matter fractional anisotropy and other indices of cerebral health in normal aging: tract-based spatial statistics study of aging. NeuroImage 2007;35:478–487. [PubMed: 17292629]

Kochunov P, Thompson PM, Coyle TR, Lancaster JL, Kochunov V, Royall D, Mangin JF, Riviere D, Fox PT. Relationship among neuroimaging indices of cerebral health during normal aging. Hum. Brain Mapp 2008;29:36–45. [PubMed: 17290369]

Kochunov P, Robin D, Royall D, Lancaster J, Kochunov V, Coyle T, Schlosser A, Fox P. Can structural MRI cerebral health markers track cognitive trends in executive control function during normal maturation and adulthood? Hum. Brain Mapp. in press.

Kraut MA, Beason-Held LL, Elkins WD, Resnick SM. The impact of magnetic resonance imaging-detected white matter hyperintensities on longitudinal changes in regional cerebral blood flow. J. Cereb. Blood Flow Metab 2008;28:190–197. [PubMed: 17534385]

Lehmbeck JT, Brassen S, Weber-Fahr W, Braus DF. Combining voxel-based morphometry and diffusion tensor imaging to detect age-related brain changes. NeuroReport 2006;17:467–470. [PubMed: 16543808]

Magnotta VA, Andreasen NC, Schultz SK, Harris G, Cizadlo T, Heckel D, Nopoulos P, Flaum M. Quantitative in vivo measurement of gyrification in the human brain: changes associated with aging. Cereb. Cortex 1999;9:151–160. [PubMed: 10220227]

Mangin JF, Riviere D, Cachia A, Duchesnay E, Cointepas Y, Papadopoulos-Orfanos D, Collins DL, Evans AC, Regis J. Object-based morphometry of the cerebral cortex. IEEE Trans. Med. Imag 2004;23:968–982.

Mazziotta JC, Toga AW, Evans A, Fox P, Lancaster J. A probabilistic atlas of the human brain: theory and rationale for its development. The International Consortium for Brain Mapping (ICBM). NeuroImage 1995;2:89–101. [PubMed: 9343592]

Meyers, J.; Meyers, K. Psychological Assessment Resources. Odessa, Fla.: 1995. Rey-Osterrieth Complex Figure and the Recognition Trial: Professional Manual.

Mielke R, Kessler J, Szelies B, Herholz K, Wienhard K, Heiss WD. Normal and pathological aging—findings of positron-emission-tomography. J. Neural Transm 1998;105:821–837. [PubMed: 9869321]

Morrison JH, Hof PR. Life and death of neurons in the aging brain. Science 1997;278:412–419. [PubMed: 9334292]

Mosconi L, Tsui WH, Herholz K, Pupi A, Drzezga A, Lucignani G, Reiman EM, Holthoff V, Kalbe E, Sorbi S, Diehl-Schmid J, Perneczky R, Clerici F, Caselli R, Beuthien-Baumann B, Kurz A, Minoshima S, de Leon MJ. Multicenter standardized 18F-FDG pet diagnosis of mild cognitive impairment, Alzheimer's disease, and other dementias. J. Nucl. Med 2008;49:390–398. [PubMed: 18287270]

Moseley M. Diffusion tensor imaging and aging — a review. NMR Biomed 2002;15:553–560. [PubMed: 12489101]

Mueller SG, Weiner MW, Thal LJ, Petersen RC, Jack C, Jagust W, Trojanowski JQ, Toga AW, Beckett L. The Alzheimer's disease neuroimaging initiative. Neuroimaging Clin. N. Am 2005;15:869–877. [PubMed: 16443497]xi–xii.

Osborne J, Costello A. Sample size and subject to item ratio in principal components analysis. Pract. Assess., Res. Eval 2004;9

Pantoni L, Garcia JH. The significance of cerebral white matter abnormalities 100 years after Binswanger's report. A review. Stroke 1995;26:1293–1301.

Park HJ, Lee JD, Chun JW, Seok JH, Yun M, Oh MK, Kim JJ. Cortical surface-based analysis of 18F-FDG PET: measured metabolic abnormalities in schizophrenia are affected by cortical structural abnormalities. NeuroImage 2006;31:1434–1444. [PubMed: 16540349]

Pierpaoli C, Basser PJ. Toward a quantitative assessment of diffusion anisotropy. Magn. Reson. Med 1996;36:893–906. [PubMed: 8946355]

Raichle ME. Measurement of local cerebral blood flow and metabolism in man with positron emission tomography. Fed. Proc 1981;40:2331–2334. [PubMed: 6972328]

Raz N, Gunning FM, Head D, Dupuis JH, McQuain J, Briggs SD, Loken WJ, Thornton AE, Acker JD. Selective aging of the human cerebral cortex observed in vivo: differential vulnerability of the prefrontal gray matter. Cereb. Cortex 1997;7:268–282. [PubMed: 9143446]

Raz N, Rodrigue KM, Kennedy KM, Head D, Gunning-Dixon F, Acker JD. Differential aging of the human striatum: longitudinal evidence. AJNR Am. J. Neuroradiol 2003;24:1849–1856. [PubMed: 14561615]

Reiman EM, Caselli RJ, Chen K, Alexander GE, Bandy D, Frost J. Declining brain activity in cognitively normal apolipoprotein E epsilon 4 heterozygotes: a foundation for using positron emission tomography to efficiently test treatments to prevent Alzheimer's disease. Proc. Natl. Acad. Sci. U. S. A 2001;98:3334–3339. [PubMed: 11248079]

Salat DH, Tuch DS, Greve DN, van der Kouwe AJ, Hevelone ND, Zaleta AK, Rosen BR, Fischl B, Corkin S, Rosas HD, Dale AM. Age-related alterations in white matter microstructure measured by diffusion tensor imaging. Neurobiol. Aging 2005;26:1215–1227. [PubMed: 15917106]

Small GW. Diagnostic issues in dementia: neuroimaging as a surrogate marker of disease. J. Geriatr. Psychiatry Neurol 2006;19:180–185. [PubMed: 16880360]

Small GW, Bookheimer SY, Thompson PM, Cole GM, Huang SC, Kepe V, Barrio JR. Current and future uses of neuroimaging for cognitively impaired patients. Lancet Neurol 2008;7:161–172. [PubMed: 18207114]

Smith, A. Symbol Digit Modality Test. Los Angeles: Western Psychological Services; 1991.

Smith SM. Fast robust automated brain extraction. Hum. Brain Mapp 2002;17:143–155. [PubMed: 12391568]

Smith SM, Jenkinson M, Johansen-Berg H, Rueckert D, Nichols TE, Mackay CE, Watkins KE, Ciccarelli O, Cader MZ, Matthews PM, Behrens TE. Tract-based spatial statistics: voxelwise analysis of multi-subject diffusion data. Neuro-Image 2006;31(4):1487–1505. [PubMed: 16624579]

Sullivan EV, Pfefferbaum A. Diffusion tensor imaging in normal aging and neuropsychiatric disorders. Eur. J. Radiol 2003;45:244–255. [PubMed: 12595109]

Symonds LL, Archibald SL, Grant I, Zisook S, Jernigan TL. Does an increase in sulcal or ventricular fluid predict where brain tissue is lost? J. Neuroimaging 1999;9:201–209. [PubMed: 10540599]

Tang Y, Nyengaard JR, Pakkenberg B, Gundersen HJ. Age-induced white matter changes in the human brain: a stereological investigation. Neurobiol. Aging 1997;18:609–615. [PubMed: 9461058]

ten Dam VH, van den Heuvel DM, de Craen AJ, Bollen EL, Murray HM, Westendorp RG, Blauw GJ, van Buchem MA. Decline in total cerebral blood flow is linked with increase in periventricular but not deep white matter hyperintensities. Radiology 2007;243:198–203. [PubMed: 17329688]

Thal LJ. Prevention of Alzheimer disease. Alzheimer Dis. Assoc. Disord 2006;20:S97–S99. [PubMed: 16917204]

Thompson PM, Hayashi KM, de Zubicaray G, Janke AL, Rose SE, Semple J, Herman D, Hong MS, Dittmer SS, Doddrell DM, Toga AW. Dynamics of gray matter loss in Alzheimer's disease. J. Neurosci 2003;23:994–1005. [PubMed: 12574429]

Thompson PM, Hayashi KM, Sowell ER, Gogtay N, Giedd JN, Rapoport JL, de Zubicaray GI, Janke AL, Rose SE, Semple J, Doddrell DM, Wang Y, van Erp TG, Cannon TD, Toga AW. Mapping cortical change in Alzheimer's disease, brain development, and schizophrenia. NeuroImage 2004;23:DS2–DS18.

Tiffin, J. Purdue Pegboard: Examiner Manual. Chicago: Science Research Associates; 1968.

Ulug AM, Barker PB, van Zijl PC. Correction of motional artifacts in diffusion-weighted images using a reference phase map. Magn. Reson. Med 1995;34:476–480. [PubMed: 7500889]

Wechsler, D. WAIS-III Administration and Scoring Manual. San Antonio: Psychological Corporation; 1997.

Wen W, Sachdev PS, Chen X, Anstey K. Gray matter reduction is correlated with white matter hyperintensity volume: a voxel-based morphometric study in a large epidemiological sample. NeuroImage 2006;29:1031–1039. [PubMed: 16253521]

Wilkins A, Chandran S, Compston A. A role for oligodendrocyte-derived IGF-1 in trophic support of cortical neurons. Glia 2001;36:48–57. [PubMed: 11571783]

Wilkins A, Majed H, Layfield R, Compston A, Chandran S. Oligodendrocytes promote neuronal survival and axonal length by distinct intracellular mechanisms: a novel role for oligodendrocyte-derived glial cell line-derived neurotrophic factor. J. Neurosci 2003;23:4967–4974. [PubMed: 12832519]

Witelson SF. Hand and sex differences in the isthmus and genu of the human corpus callosum. A postmortem morphological study. Brain 1989;112(Pt 3):799–835. [PubMed: 2731030]

Yanase D, Matsunari I, Yajima K, Chen W, Fujikawa A, Nishimura S, Matsuda HMY. Brain FDG PET study of normal aging in Japanese: effect of atrophy correction. Eur. J. Nucl. Med. Mol. Imaging 2005;32(7):794–805. [PubMed: 15759148]

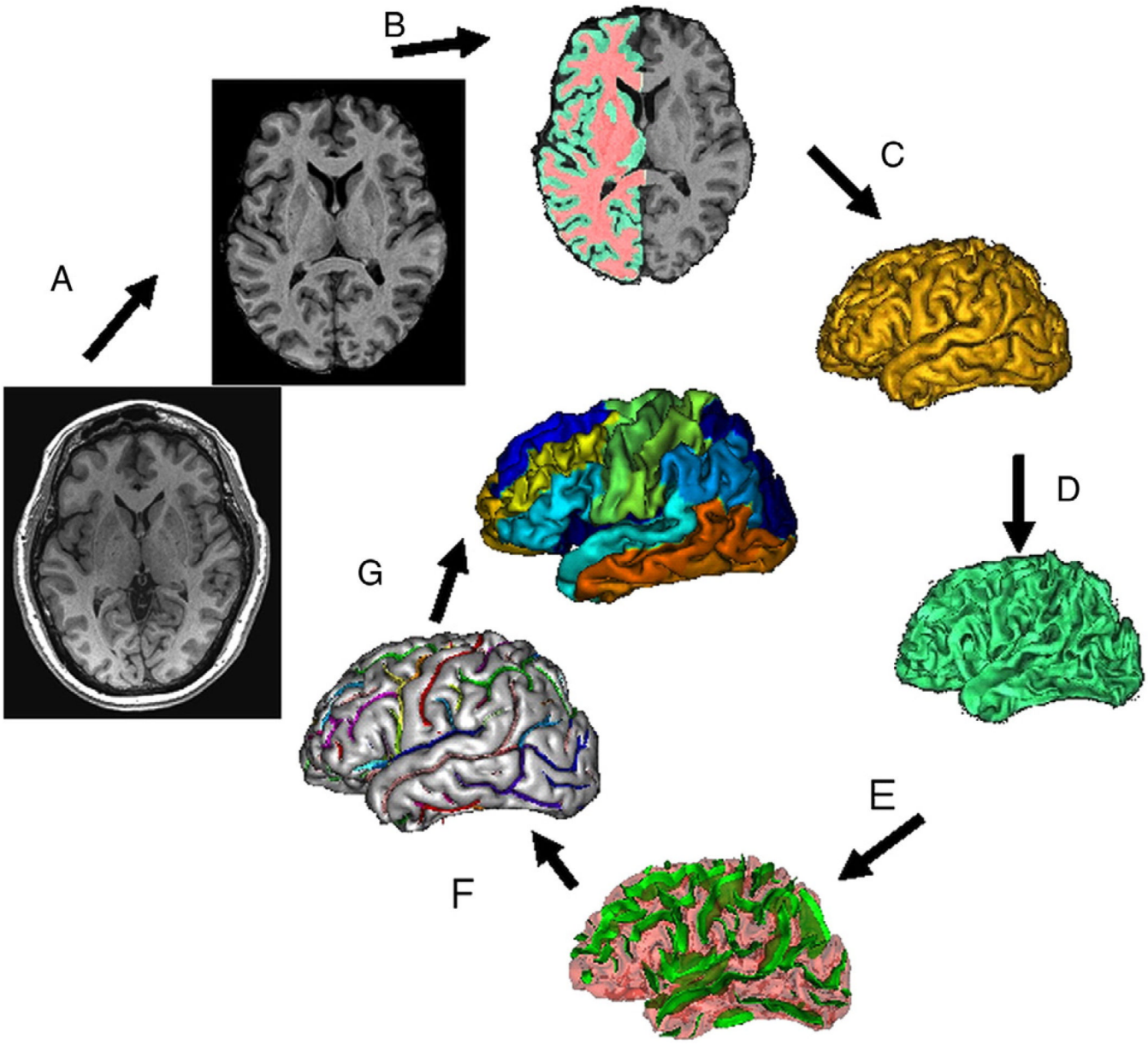


**Fig. 1.**

T1-w image processing pipelines. A T1-w image is skull-stripped, globally spatially normalized, and RF-inhomogeneity corrected (A). Next, cerebral hemispheres and cerebellum and identified and tissue classified (B); cortical surfaces for GM and WM are calculated (C, D) and homotopic erosion operation and crevasse detector are used to reconstruct sulcal surface as the medial surface of the two opposing gyral banks (E). Sulcal identification pipeline uses a congregation of 500 artificial neural network-based pattern classifiers to identify (F) sulcal landmarks and to perform gyral segmentation of the cortex (G).

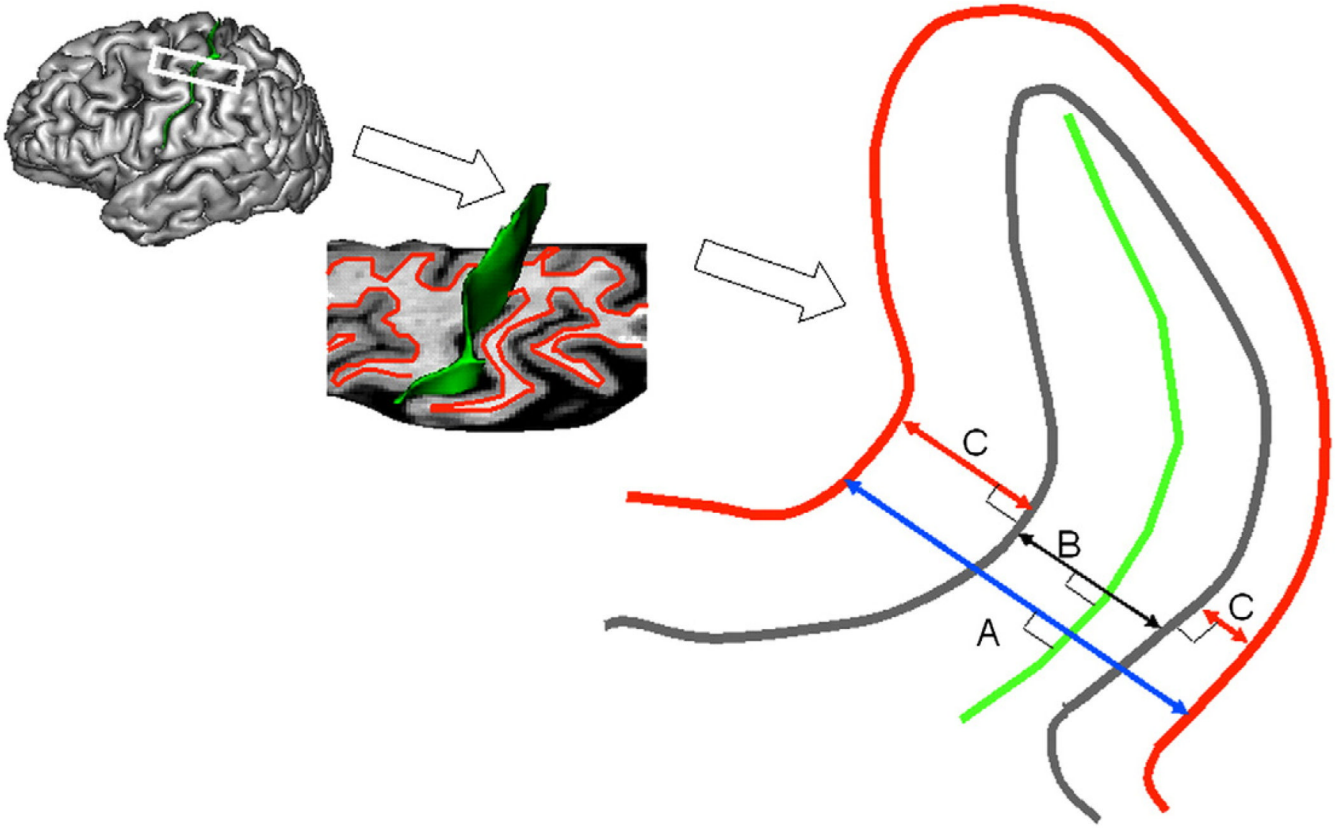


**Fig. 2.**

Cortical markers of cerebral integrity. T1-w image processing pipeline (Fig. 1) produced sulcal surface (green) and pial GM (gray) and inner WM (red) surfaces. For each sulcus three average measurements of cortical cerebral integrity are computed: average intergyral (A), sulcal (B) spans and average GM thickness (C). Intergyral span (A) is defined as the 3-D distance between opposing points on the WM mesh along the normal projection to the sulcal surface. Sulcal span (B) is defined as a 3D distance between opposing points on the GM mesh along the normal projections to the sulcal surface. Gyral GM thickness (C) is defined as a distance between pial GM and inner WM meshes at the direction normal to the pial GM surface. These measurements are calculated for every vertex of the sulcal surface resulting in averaging of ~2–5000 measurements for each sulcus.

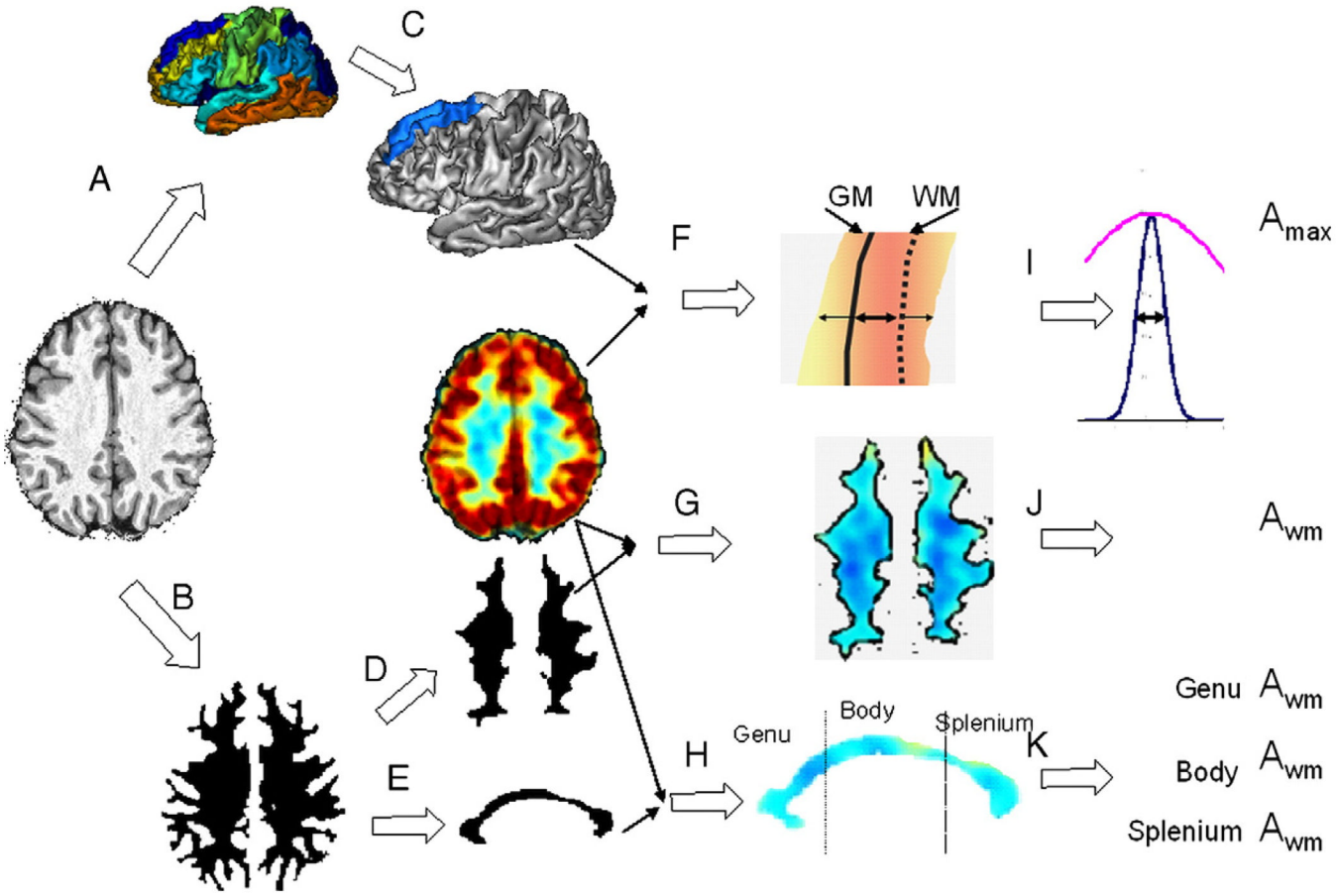


**Fig. 3.**

Extraction of regional FDG PET measurements. Anatomical images were processed with BV pipeline that produced cortical parcelation maps (A) and mask of cerebral WM (B). For each gyrus/cortical area (C), crossectional FDG intensity and WM/GM distance were analyzed to measure peak intensity $A'_{max}$ and GM thickness (F, I). These measurements were performed for each of the nodes of the gyrus (~10000) and results were averaged. The cerebral WM mask was eroded (D) to measure $A_{wm}$, average WM activity. The mask of the corpus callosum (CC) was eroded (E) to measure $A_{wm}$ for genu, body and splenium of CC.

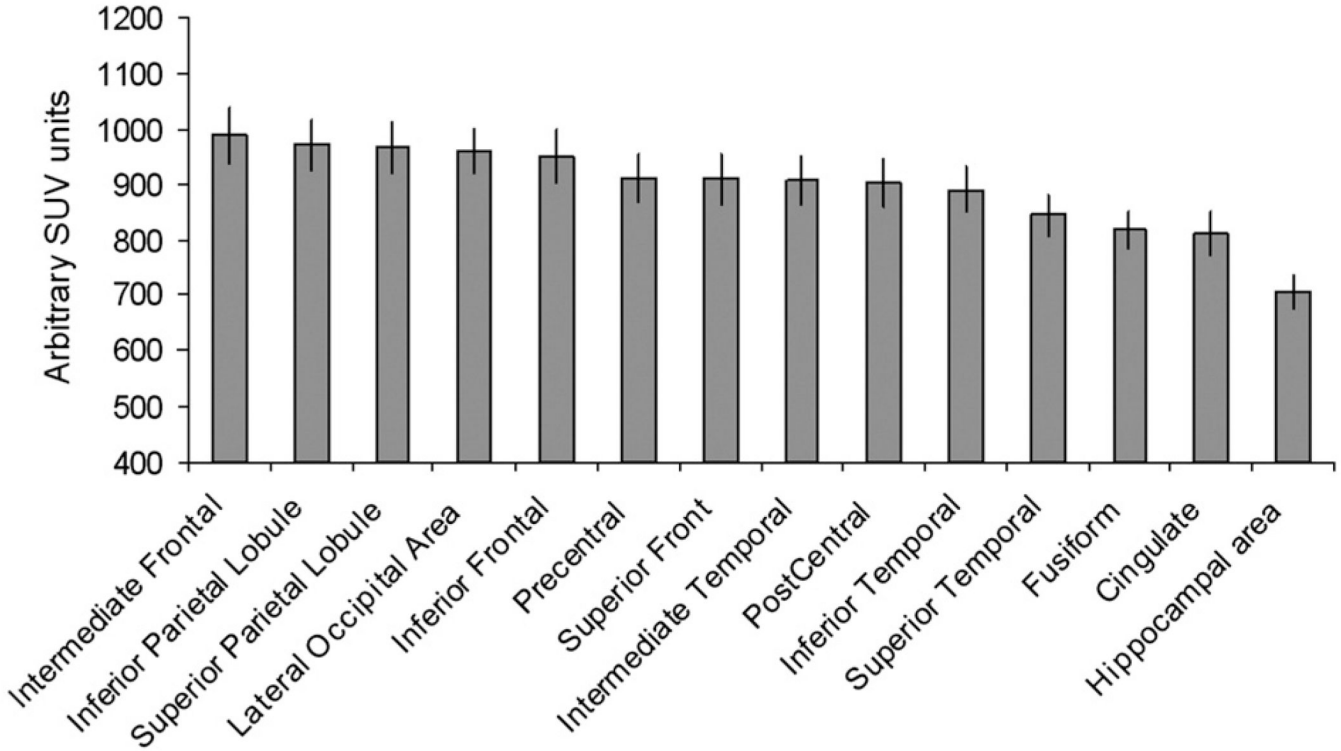


**Fig. 4.**
Baseline FDG uptake values (average $A_{max}$) for 14 cortical gyri/areas.

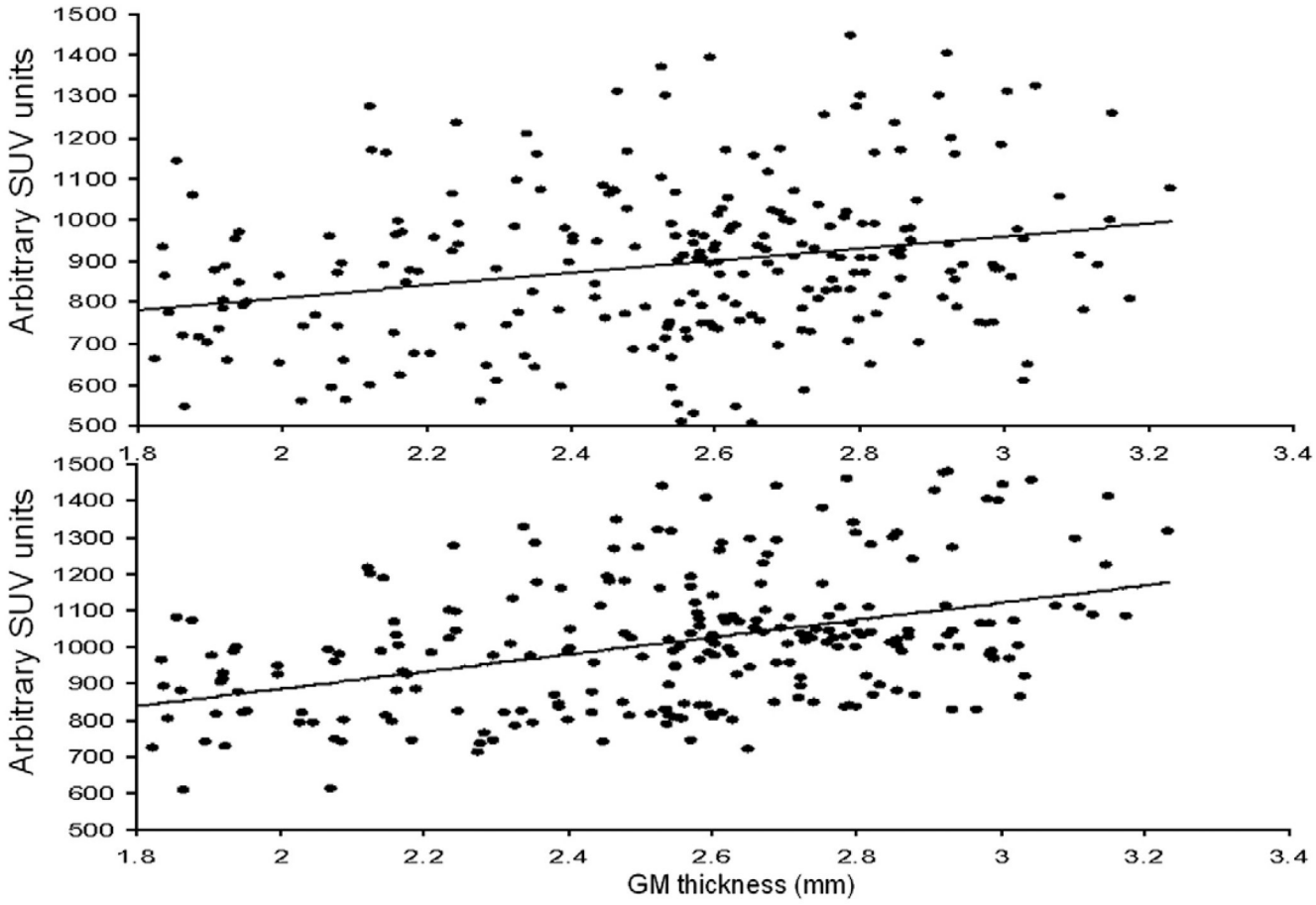


**Fig. 5.**

Cortical FDG uptake ($A_{max}$) values for 14 cortical gyri/areas plotted vs. GM thickness for 19 subjects before (top) and after intensity normalization (bottom) that normalized the average FDG intensity for every gyrus/area.

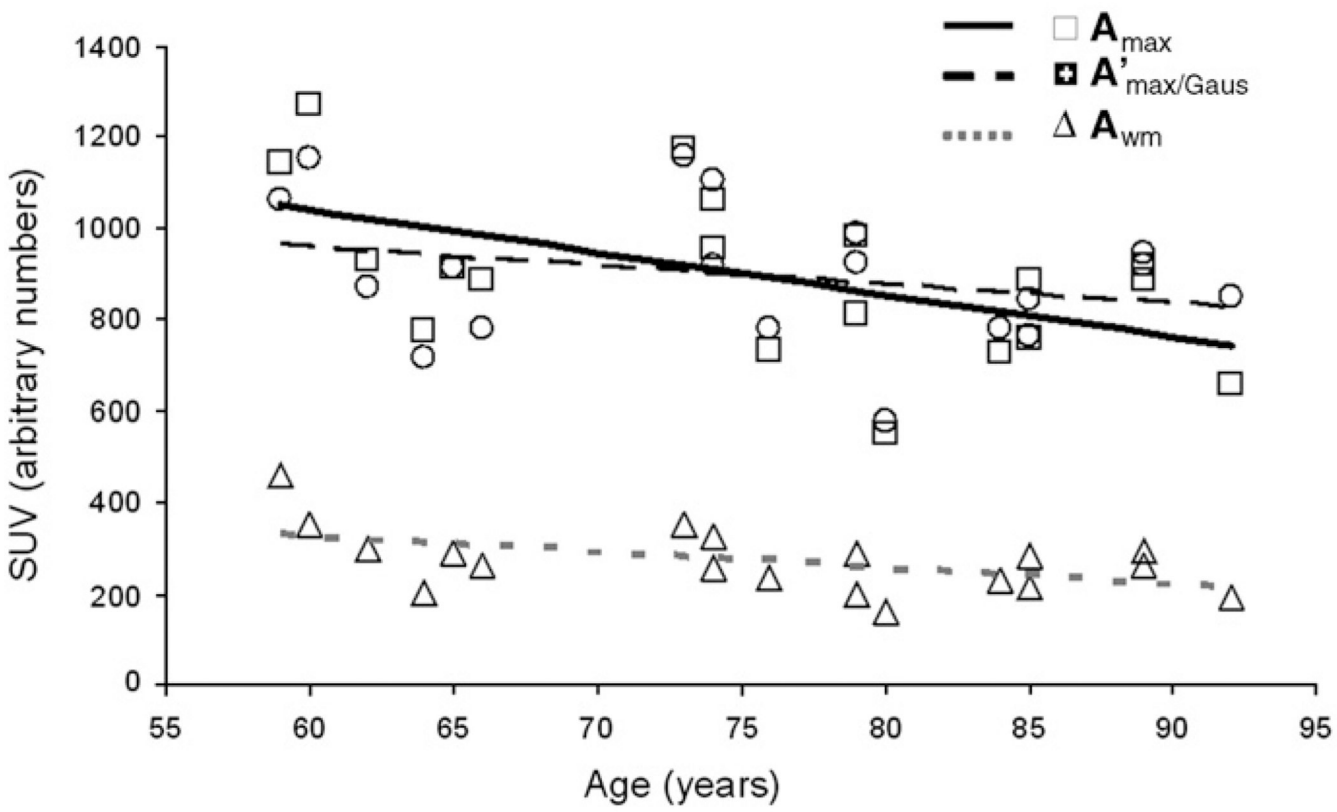


**Fig. 6.**
Whole-brain cerebral metabolism markers plotted vs. age. Regression lines are shown for uncorrected cortical GM (solid), corrected cortical GM (interrupted) and cerebral WM (shaded, dotted) average FDG uptake values.

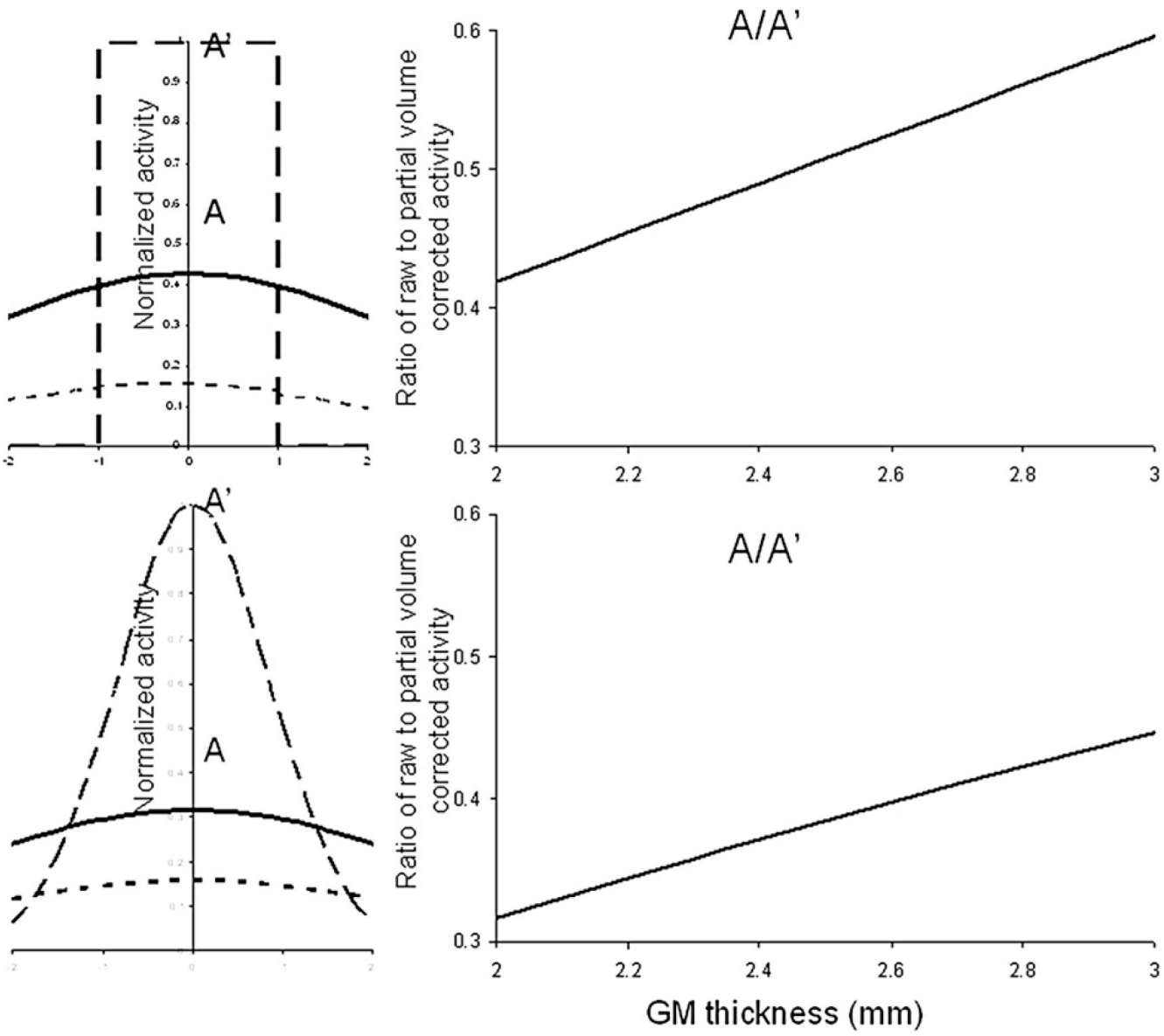


**Fig. S1.**
Partial voxel averaging correction was modeled using rectangular (top) and Gaussian (bottom) approximations. The graphs are shown for FWHM of the PET camera set at 6 mm.

**Table 1**

Column 1, sulcal and intergyral spans were calculated for 12 primary and secondary sulcal structures per hemisphere

| **Sulcal structures** | **Cortical areas** |
|---|---|
| Superior frontal sulcus | Superior frontal |
| Inferior frontal sulcus | Intermediate frontal |
| Pre-central sulcus | Inferior frontal |
| Postcentral sulcus | Pre central |
| Intraparietal fissure | Post central |
| Superior temporal sulcus | Superior parietal lobule |
| Cingulate sulcus | Inferior parietal lobule |
| Lateral and transverse occipital and lunate sulci | Lateral occipital area |
| Calcarine fissure | Superior temporal |
| Central sulcus | Intermediate temporal |
| Parietaloccipital fissure | Inferior temporal |
| Collateral sulci | Cingulate |
| | Fusiform |
| | Hippocampal area |

Column 2, GM thickness and FDG PET standard uptake values were calculated for 14 gyral and cortical areas per hemisphere.

**Table 2**

Average surface area, cortical GM thickness, $A_{max}$ and its standard error of the mean (SEM), correlation coefficients between gyral average $A'_{max}$ and gyral average GM thickness calculated using rectangular and Gaussian approximations and their SEM values are shown for 14 gyri/cortical areas

| Cortical areas | Area ($mm^2$) | GM thickness (mm) | $A_{max}$ (uptake units) | $A_{max}$ SEM % of mean | $r$ (rect. profile) | $r$ (Gaus. profile) | $A'_{max}$ SEM % of mean (Rect) | $A'_{max}$ SEM % of mean (Gaus) |
|---|---|---|---|---|---|---|---|---|
| Superior frontal | 4750±200 | 2.7±.05 | 910 | 5.4 | .48 | .53 | 4.0 | 3.9 |
| Intermediate frontal | 3770±250 | 2.6±.05 | 995 | 6.0 | .46 | .51 | 4.6 | 4.5 |
| Inferior frontal | 3200±140 | 2.6±.06 | 951 | 5.6 | .46 | .5 | 4.3 | 4.3 |
| Pre central | 6090±140 | 2.5±.06 | 912 | 5.1 | .52 | .53 | 3.7 | 3.7 |
| Post central | 4610±150 | 2.1±.05 | 902 | 5.0 | .55 | .55 | 3.5 | 3.5 |
| Superior parietal lobule | 8130±280 | 2.1±.05 | 966 | 5.4 | .51 | .53 | 3.9 | 3.9 |
| Inferior parietal lobule | 5670±275 | 2.3±.07 | 972 | 5.4 | .57 | .58 | 3.8 | 3.8 |
| Lateral Occipital area | 2830±230 | 2.0±.06 | 960 | 4.8 | .44 | .45 | 3.9 | 3.8 |
| Superior temporal | 4040±200 | 2.6±.07 | 840 | 4.5 | .45 | .47 | 3.4 | 3.4 |
| Intermediate temporal | 4650±250 | 2.6±.07 | 880 | 5.0 | .46 | .51 | 3.8 | 3.8 |
| Inferior temporal | 2970±180 | 2.6±.08 | 890 | 4.9 | .46 | .51 | 3.8 | 3.7 |
| Cingulate | 4790±290 | 2.5±.07 | 810 | 4.7 | .52 | .55 | 3.4 | 3.4 |
| Fusiform | 2120±150 | 2.7±.07 | 820 | 3.9 | .56 | .60 | 2.8 | 2.8 |
| Hippocampal area | 1700±200 | 2.6±.08 | 705 | 3.7 | .52 | .57 | 2.7 | 2.7 |

**Table 3**

Correlation coefficients between whole brain functional and structural indices of cerebral integrity and age

| FA | GM thickness | Sulcal Span | $A_{max}$ | $A_{wm}$ | $A'_{max/Rect}$ | $A'_{max/Gaus}$ | Intergyral span | HWM volume |
|---|---|---|---|---|---|---|---|---|
| −.80* | −.67* | .59* | −.54* | −.51* | −.27 | −.28 | .41 | .38 |

* Indicated statistically significant correlation ($p$<.05).

**Table 4**

Age-corrected partial correlation coefficients between $^{18}$FDG PET uptake values and MR-based indices of cerebral integrity

| FDG PET index | GM thickness | FA | HWM volume | Sulcal Span | Intergyral span |
|---|---|---|---|---|---|
| $A_{max}$ | .32 | .32 | −.48* | −.21 | −.51* |
| $A'_{max\ Rect}$ | .01 | .33 | −.55* | −.24 | −.54* |
| $A'_{max\ Gaus}$ | .01 | .33 | −.56* | −.24 | −.55* |
| $A_{wm}$ | .02 | .10 | −.36 | −.42 | −.52* |

* Indicated statistically significant correlation ($p$<.05).

**Table 5**

Correlation coefficients for gyral $^{18}$FDG PET uptake values with age and partial age-corrected correlation coefficients with other indices of cerebral integrity for 14 cortical gyri/areas

| Cortical Areas | FDG PET measurements | Age | GM thickness | FA | HWM volume | Sulcal span | Intergyral span |
|---|---|---|---|---|---|---|---|
| Superior frontal | $A_{max}$ | −.52* | .20 | .21 | −.43 | −.29 | −.46* |
| | $A'_{max/Gaus}$ | −.35 | .11 | .23 | −.49* | −.36 | −.43 |
| Intermediate | $A_{max}$ | −.54* | .26 | .25 | −.43 | −.28 | −.48* |
| frontal | $A'_{max/Gaus}$ | −.37 | −.05 | .29 | −.51* | −.34 | −.49* |
| Inferior frontal | $A_{max}$ | −.51* | .29 | .23 | −.43 | −.20 | −.44 |
| | $A'_{max/Gaus}$ | −.33 | .11 | .24 | −.54* | −.36 | −.51* |
| Pre central | $A_{max}$ | −.54* | .25 | .24 | −.44 | −.21 | −.50* |
| | $A'_{max/Gaus}$ | −.25 | −.15 | .25 | −.52* | −.39 | −.50* |
| Post central | $A_{max}$ | −.53* | .29 | .30 | −.48* | −.15 | −.50* |
| | $A'_{max/Gaus}$ | −.22 | .09 | .36 | −.54* | −.30 | −.49* |
| Superior | $A_{max}$ | −.54* | .33 | .27 | −.40 | −.16 | −.46* |
| parietal lobule | $A'_{max/Gaus}$ | −.25 | .02 | .29 | −.46* | −.31 | −.54* |
| Inferior parietal | $A_{max}$ | −.56* | .31 | .28 | −.40 | −.14 | −.41 |
| lobule | $A'_{max/Gaus}$ | −.12 | −.10 | .20 | −.46* | −.39 | −.52* |
| Lateral Occipital | $A_{max}$ | −.45* | .43 | .36 | −.38 | −.12 | −.41 |
| area | $A'_{max./Gaus}$ | −.19 | .09 | .30 | −.44 | −.26 | −.51* |
| Superior | $A_{max}$ | −.55* | .29 | .29 | −.51* | −.15 | −.49* |
| temporal | $A'_{max/Gaus}$ | −.25 | −.14 | .23 | −.60* | −.36 | −.50* |
| Intermediate | $A_{max}$ | −.52* | .28 | .31 | −.50* | −.14 | −.49* |
| temporal | $A'_{max/Gaus}$ | −.25 | −.09 | .29 | −.62* | −.25 | −.56* |
| Inferior | $A_{max}$ | −.49* | .31 | .32 | −.44 | −.15 | −.49* |
| temporal | $A'_{max/Gaus}$ | −.25 | −.09 | .30 | −.58* | −.18 | −.52* |
| Cingulate | $A_{max}$ | −.57* | .31 | .30 | −.46* | −.18 | −.48* |
| | $A'_{max/Gaus}$ | −.42 | −.04 | .19 | −.46* | −.29 | −.52* |
| Fusiform | $A_{max}$ | −.50* | .39 | .30 | −.42 | −.15 | −.51* |
| | $A'_{max/Gaus}$ | −.21 | −.10 | .21 | −.52* | −.25 | −.52* |
| Hippocampal | $A_{max}$ | −.60* | .23 | .29 | −.49* | −.10 | −.57 |

| Cortical Areas | FDG PET measurements | Age | GM thickness | FA | HWM volume | Sulcal span | Intergyral span |
|---|---|---|---|---|---|---|---|
| area | $A'_{max/Gaus}$ | −.39 | −.15 | .35 | −.60* | −.11 | −.54* |

*Indicates statistically significant correlation ($p$<.05).

**Table 6**

Correlation between average $^{18}$FDG PET uptake values for three regions of corpus callosum and age

| **Genu $A_{wm}$** | **Body $A_{wm}$** | **Splenium $A_{wm}$** |
|---|---|---|
| −.63* | −.30 | −.34 |

* Indicated statistically significant correlation ($p<.05$).

**Table 7**

Age-corrected partial correlation coefficients between average $^{18}$FDG PET uptake values for the three regions of CC and other indices of cerebral integrity

| CC Regional $A_{wm}$ values | GM thickness | FA | HWM volume | Sulcal Span | Intergyral span |
|---|---|---|---|---|---|
| Genu | .42 | .49* | −.62* | −.24 | −.58* |
| Body | .23 | .41 | −.56* | .03 | −.56* |
| Splenium | .21 | .50* | −.60* | −.21 | −.56* |

*Indicated statistically significant correlation ($p$<.05). *indicates significant ($p$<.05) age-correction partial correlations.